agriculture

MDPI

Article

CFD Optimization of Air Supply Angle and Rack Layout for Straw Mushroom

Chuanqing Wang [1,2], Shao Li [1,2,*], Xiaoming Ding [1,2], Chunhui Wang [1,2], Guanshan Zhang [3], Yuefeng Chen [4] and Xijia Xu [5]

[1] Academy of Agricultural Planning and Engineering, Ministry of Agriculture and Rural Affairs, Beijing 100125, China
[2] Key Laboratory of Farm Building in Structure and Intelligent Construction, Ministry of Agriculture and Rural Affairs, Beijing 100125, China
[3] College of Mechanical and Electronic Engineering, Shandong Agricultural University, Taian 271018, China
[4] Zhejiang Branch of Chinese Academy of Agricultural Mechanization Sciences Group Co., Ltd., Shaoxing 312039, China
[5] Shaoguan Starway Bio-Technology Co., Ltd., Shaoguan 512136, China
* Correspondence: lishao@aape.org.cn

Abstract

Air distribution uniformity is critical to the quality and yield of straw mushrooms (*Volvariella volvacea*); however, the coupled effects of air supply angle and cultivation rack layout remain poorly understood. We developed and validated a steady-state CFD model for a straw mushroom house with an active return-air heat pump system. Model validation against field measurements showed mean relative errors of 7.2%, 9.5%, and 1.1% for in-duct velocity, outlet velocity, and temperature, respectively confirming reliability of the model. Four scenarios were then simulated, combining horizontal (0°), vertical (90°), and mixed supply angles with two or three rack rows. The two-row layout with vertical downward supply (2-90°) achieved the best overall performance, attaining a vertical velocity CV of 8.7% and optimal-zone area ratios of approximately 90% across all layers. The mixed supply (2-0°+90°) showed intermediate performance (vertical velocity CV = 13.7%), whereas the horizontal cases (2-0° and 3-0°) exhibited pronounced wall-attachment effects, with vertical velocity CVs of 42.2% and 26.7%, respectively. An AHP-entropy-weighted TOPSIS evaluation further confirmed the superiority of the schemes incorporating a vertical component, with 2-90° ranking highest. These findings indicate that vertical downward supply combined with a two-row layout markedly improves environmental uniformity, providing practical guidance for the ventilation design of similar intensive mushroom cultivation facilities.

Keywords: straw mushroom growing house; CFD simulation; air supply angle; cultivation rack layout; airflow uniformity

Check for updates

Academic Editor: Ju-Seok Nam

Received: 10 August 2026
Revised: 27 September 2026
Accepted: 14 October 2026
Published: 16 October 2026

Copyright: © 2026 by the authors. Licensee MDPI, Basel, Switzerland. This article is an open access article distributed under the terms and conditions of the Creative Commons Attribution (CC BY) license.

1. Introduction

Edible mushrooms are valued for their low calorie content, high dietary fiber, and medicinal properties. China is the world's largest producer of edible mushrooms, accounting for approximately 85% of the global output [1]. Modern cultivation facilities are designed to provide optimal environmental conditions for different growth stages. With the trend toward large-scale and industrial production, growing houses have become progressively larger, imposing higher demands on ventilation components and control systems [2,3]. However, improperly designed ventilation systems may impede air circulation

and cause uneven internal microclimates, leading to the accumulation of heat, water vapor, and CO_2 in the cultivation zone; this in turn inhibits normal mushroom development and reduces both product quality and yield [4,5].

The straw mushroom (*Volvariella volvacea*) is a typical high-temperature and high-humidity species originally cultivated in southern China [6]. Its growth cycle comprises two phases: mycelial growth and fruiting body differentiation. The mycelial phase requires 30–35 °C and approximately 70% relative humidity, while fruiting body development requires 28–34 °C and 85–95% relative humidity [7]. When CO_2 concentration exceeds 1000 ppm, toxic effects on fruiting bodies occur [8]. Therefore, adequate and uniform ventilation during the fruiting stage is critical for maintaining proper temperature, humidity, and CO_2 levels.

Appropriate ventilation design is a critical prerequisite for ensuring the normal growth of the straw mushroom, and extensive studies have been conducted on this topic [9,10]. Peng et al. [11] investigated the airflow organization of a side-wall upper-supply and single-wall return configuration using CFD simulation, and reported that the optimal air supply angle was 55–60° at a velocity of 6.0 m/s. Zheng et al. [12] determined the natural ventilation strategy for straw mushroom growing houses during transitional seasons based on CFD calculations, recommending ventilation every 70 min with each session lasting approximately 12 min. Cheng et al. [13] analyzed the influence of air duct position on airflow and temperature distributions inside straw mushroom growing houses. In recent years, the application of CFD simulation has expanded from straw mushroom to other cultivated species, such as *Hypsizygus marmoreus* and *Flammulina filiformis* [14–16]. However, most of the above studies focused on dual-duct or conventional duct systems, such as side-wall slot supply and single-wall louver return, primarily addressing the adjustment of air supply angles [17,18]. For active return-air systems, the effect of the air supply angle on airflow distribution and environmental uniformity has not been systematically investigated. The cultivation rack layout is another key factor influencing airflow distribution and cooling efficiency. Lee et al. [19] used CFD to examine the effect of multi-tier cultivation racks on the microclimate in a mushroom growing house, finding that a rational layout significantly improved indoor airflow distribution. Li et al. [20] investigated horizontal spacing between cultivation racks in a mushroom solar greenhouse and identified 0.8 m as the optimum. However, these studies concentrated on continuous adjustments of horizontal spacing and did not address the implications of changing the number of rack rows. In practice, altering the number of rows changes not only aisle width but also jet trajectories and vortex structures [19,21]. Therefore, the coupled effects of supply angle and rack row number in active return-air systems merit further investigation.

To address this gap, we developed and field-validated a steady-state CFD model of a straw mushroom growing house equipped with an active return-air system. Four scenarios combining two supply angles (0° horizontal and 90° vertical) and two rack row counts (two and three) were systematically compared. This study makes three specific contributions: (i) it quantifies the coupled influence of supply angle and rack row number on velocity and temperature uniformity; (ii) it reveals the physical mechanisms underlying the performance differences, including wall-attachment effects and jet impingement-driven inter-layer mixing; and (iii) it provides a multi-criteria optimal scheme via an AHP-entropy-weighted TOPSIS evaluation. The findings offer quantitative design guidance for ventilation systems in similar intensive mushroom cultivation facilities.

2. Materials and Methods

2.1. Experimental Site and Materials

The experiment was conducted in April 2026 at a straw mushroom production base in Zhangshi Town, Shaoguan City, Guangdong Province. The experimental facility was a straw mushroom growing house, which was a white shaded arched polyethylene-polyester (PEP) plastic tunnel with a length of 19.0 m, width of 5.0 m, sidewall height of 2.5 m, and ridge height of 3.0 m. The structure comprised a steel frame covered externally with a 0.12-mm-thick black–white PEP film, a middle layer of spray-bonded cotton insulation quilt, and an inner layer of 0.1 mm thick PO film.

The growing house was equipped with an active return-air fresh air heat pump system. Supply air was delivered through a centrally located longitudinal cylindrical polyethylene air duct (length 18.5 m, diameter 0.4 m) suspended from the ceiling. The duct had evenly distributed supply holes with a diameter of 50 mm at a spacing of 33.0 cm. The system had a maximum supply air rate of 10,000 m^3/h, a maximum exhaust rate of 5000 m^3/h, a power consumption of 18.0 kW, a fan static pressure of 500 Pa, a cooling capacity of 40.0 kW, a heating capacity of 42.0 kW, and a heat recovery efficiency of 68%. The active return-air inlet had dimensions of 0.5 m (width) × 0.7 m (height) (Figure 1).



Figure 1. Schematic of the active return-air fresh air heat pump system.

Four cultivation racks were arranged on both the left and right sides of the house, with four layers on each side. The lowest layer was 0.2 m above the floor. Each layer was 17.0 m long and 1.0 m wide, with a vertical spacing of 0.6 m. The substrate thickness was 18.0 cm. The distance between the racks and the sidewall was 0.7 m, and the spacing between the two central racks was 1.6 m (Figure 2).



Figure 2. Layout of cultivation racks inside the growing house.

Measurements were taken at 10:00 a.m. on 24 April 2026. Air velocity and static pressure inside the air duct were measured at nine cross-sections spaced every 2 m along the duct, with the measuring point located at the duct center. Indoor temperature and humidity were monitored at two horizontal planes (0.5 m and 1.7 m above the floor), with four points per plane (one on each side in the width direction and two evenly spaced along the length direction), giving a total of eight points (Figure 3a). Figure 3b shows the full layout of the temperature monitoring points and the nine duct cross-sections.

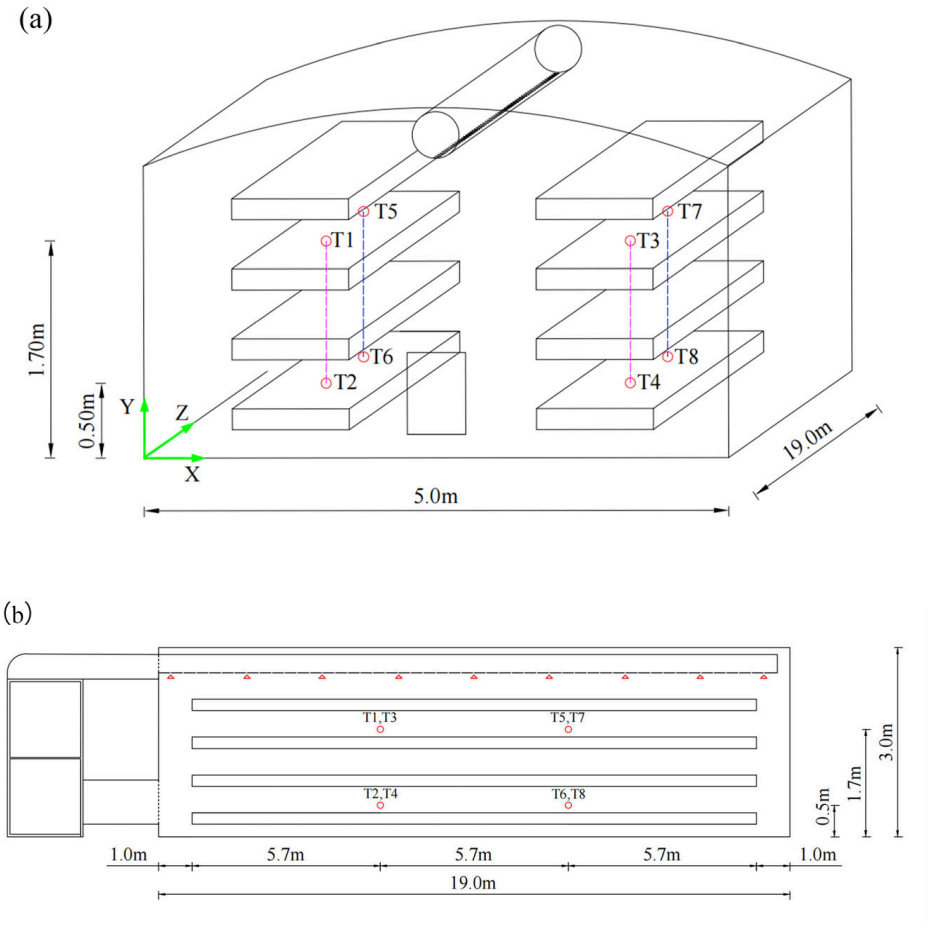


Figure 3. Measurement system layout: (**a**) perspective view; (**b**) side view showing duct cross-sections (triangles) and temperature monitoring points.

A multifunctional detection system (YIOU DP7000A, Shanghai, China, range: 0–500 Pa, 0–30.0 m/s, –50.0–100.0 °C, accuracy ±0.5%, probe length 40 cm) and a hot-wire anemometer (Testo 405i, Titisee-Neustadt, Germany, resolution ±0.1 m/s) were used to measure the in-duct and supply-hole air velocities, respectively. Indoor temperature and relative humidity were continuously recorded at 10 min intervals using HOBO UX100-003 data loggers (Bourne, MA, USA, temperature accuracy ±0.21 °C, range −20–70 °C; relative humidity accuracy 3.5%, range 15–95%), with the average values used for subsequent calculations. Wall surface temperatures were measured with a Fluke 63 infrared thermometer (Everett, WA, USA, range −32–535 °C, accuracy ±1 °C). Photographs of the experimental facility and measurement setup are provided in the Supplementary Materials (Figure S1).

2.2. Numerical Modeling

In this study, all simulations were performed using ANSYS Fluent 2024 R1 (ANSYS, Inc., Canonsburg, PA, USA). The three-dimensional geometry was created and meshed in

ANSYS ICEM CFD 2024 R1, and the simulation results were post-processed and visualized using ANSYS CFD-Post 2024 R1.

2.2.1. Mathematical Model

The airflow inside the straw mushroom growing house satisfies the three fundamental conservation laws: continuity, momentum conservation, and energy conservation. In this study, indoor air was treated as a steady-state incompressible Newtonian fluid. The governing equations can be expressed in the following general form:

$$\frac{\partial(\rho\varphi)}{\partial t} + \frac{\partial(\rho u_j)}{\partial x_j} = \frac{\partial}{\partial x_j}(\Gamma_\varphi \frac{\partial \varphi}{\partial x_j}) + S_\varphi \quad (1)$$

where φ is the generalized variable, ρ is the air density (kg·m^{-3}), u_j is the velocity vector (m·s^{-1}), Γ_φ is the generalized diffusion coefficient, and S_φ is the source term.

Since the indoor air is a mixture of water vapor and dry air, the species transport equation must also be satisfied. For the present single-phase (humid air) assumption, the transport of water vapor is governed by the following species conservation equation [10,20]:

$$\frac{\partial}{\partial t}(\rho Y_i) + \nabla\cdot(\rho v Y_i) = -\nabla\cdot\overline{J_i} + R_i + S_i \quad (2)$$

where Y_i is the mass fraction of species i, R_i is the net rate of production by chemical reaction, and S_i is the user-defined source term. The diffusion flux $\overline{J_i}$ is given by Fick's law:

$$\overline{J_i} = -(\rho D_{i,m} + \frac{\mu_t}{S_{ct}})\nabla Y_i \quad (3)$$

where $D_{i,m}$ is the diffusion coefficient of species i in the mixture, μ_t is the turbulent viscosity, and S_{ct} is the turbulent Schmidt number (taken as 0.7). In the present study, the species of interest was water vapor, and the moisture source term S_i represented the water vapor released from the cultivation substrate and mushroom transpiration. The water vapor remained in the gaseous phase throughout the domain. The species equation was coupled with the continuity, momentum, and energy equations through the following mechanisms: (a) the mixture properties (density and specific heat are mass-fraction-weighted averages of dry air and water vapor); (b) the buoyancy term in the momentum equation (via the Boussinesq approximation); and (c) the latent heat in the energy equation (through the moisture source term).

Owing to the relatively high airflow velocity and local disturbances, the flow was inevitably turbulent. The resulting Reynolds numbers at the supply inlet and at the supply holes were 1.6×10^5 and 3.0×10^4, respectively, both well above the turbulent threshold of 4000 [22,23]. In this study, the realizable k-ε turbulence model was adopted within the Reynolds-averaged Navier–Stokes (RANS) simulation framework [24]. This model describes turbulent behavior by solving the transport equations for turbulent kinetic energy (k) and turbulent dissipation rate (ε). Compared with the standard k-ε model, the realizable k-ε model offers significant improvements in handling flow features characterized by strong streamline curvature, vortices, and rotation [25,26].

The greenhouse covering materials consisted of two layers of black–white film and a sprayed-bonded cotton insulation quilt, resulting in extremely low solar radiation transmittance. Therefore, the effect of solar radiation on the indoor thermal environment was neglected in the simulation.

The cultivation substrate exerts a considerable influence on the indoor temperature and humidity distributions and cannot be ignored. In this study, the substrate region was treated as a porous medium, with the resistance to airflow represented by prescribed

resistance coefficients. The resistance effect of the porous medium on airflow was simulated by adding a velocity-dependent source term to the momentum equation, expressed using the Darcy–Forchheimer equation (a modified form of Darcy's law) as follows [4]:

$$S_c = -\left(\frac{\mu}{\alpha}u_i + C_2\frac{1}{2}\rho|u|u_i\right) \quad (4)$$

where μ is the dynamic viscosity of air (Pa·s), α is the permeability (m^2), C_2 is the inertial resistance coefficient (m^{-1}), ρ is the air density (kg/m^3), u_i is the velocity component in the i-direction (m/s), and $|u|$ is the magnitude of the velocity vector (m/s).

The viscous resistance coefficient $1/\alpha$ and inertial resistance coefficient C_2 were determined using the Ergun equation [27]:

$$\frac{1}{\alpha} = \frac{150(1-\gamma)^2}{d_P^2\gamma^3} \quad (5)$$

$$C_2 = \frac{3.5(1-\gamma)}{d_P\gamma^2} \quad (6)$$

where γ is the substrate porosity and d_P is the effective particle diameter. Based on a substrate porosity of d_P = 0.65 (derived from the measured moisture content of approximately 70%) and an effective particle diameter = 3.0 mm (consistent with the particle size range reported for mushroom cultivation substrates), the coefficients were calculated as $1/\alpha = 7.4 \times 10^8$ m^{-2} in the vertical direction. Because a plastic film beneath the substrate resulted in extremely low vertical permeability, an anisotropic porous media model was adopted, with horizontal resistance coefficients set to 7.4×10^5 and an inertial resistance coefficient of 1.5×10^3 m^{-1}.

2.2.2. Mesh Generation and Independence Verification

The entire computational domain, which comprised air inside the growing house, was used as the fluid domain. A three-dimensional geometric model was established in ANSYS ICEM, as shown in Figure 4, in which the supply inlet and return outlet were clearly marked. The computational domain was discretized using an unstructured tetrahedral mesh. In regions with large gradients of flow variables, such as the air supply holes of the duct, substrate surface, and near-wall zones, local mesh refinement was applied to enhance the simulation accuracy. A non-uniform mesh with boundary layer refinement was employed, as this is the standard practice for wall-bounded turbulent flows [28]. This approach allows fine resolution near walls and in high-gradient regions, while using coarser cells in the bulk flow region, maintaining computational efficiency without sacrificing accuracy.

To balance computational accuracy and efficiency, a mesh independence test was conducted over a range of 2 million to 10 million elements. The average velocity at the supply holes was used as the primary metric owing to its high velocity gradients. The mesh quality was monitored using the minimum orthogonal quality. The results show that, above 6 million elements, both the velocity and minimum orthogonal quality stabilized, with further refinement yielding negligible changes. Convergence was also verified for temperature and turbulent kinetic energy, with relative changes of <0.5% and <6.5%, respectively, between the 6.0 M and 10.0 M meshes. Table 1 summarizes the statistics for each mesh set. Based on these results, a 6.0-million-element mesh was adopted for subsequent simulations.

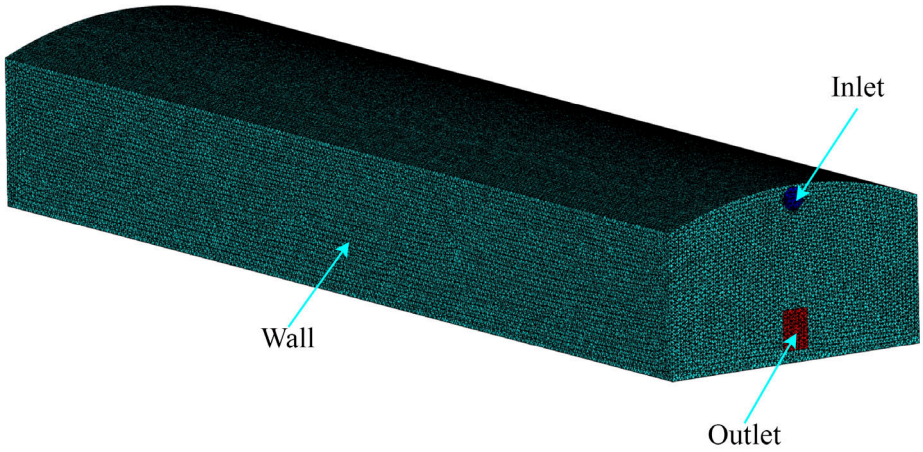


Figure 4. Unstructured tetrahedral mesh of the growing house. The supply inlet, return outlet, and wall boundaries are shown in blue, red, and green, respectively.

Table 1. Mesh model parameters.

No.	Number of Elements	Minimum Orthogonal Quality	Velocity (m/s)	Temperature (°C)	Turbulent Kinetic Energy (m^2/s^2)
Mesh 1	2.0 million	0.12	8.03	28.77	0.71
Mesh 2	4.0 million	0.27	8.54	28.53	0.84
Mesh 3	6.0 million	0.31	8.92	28.41	0.93
Mesh 4	8.0 million	0.33	8.98	28.38	0.94
Mesh 5	10.0 million	0.34	9.03	28.37	0.96

2.2.3. Boundary Conditions and Solver Settings

The boundary conditions of the computational domain were set as follows. The walls of the growing house (including the four sidewalls, the floor, and the roof) were specified as no-slip wall boundaries. The floor and internal wall surfaces were assigned the wall temperatures measured in the field experiment. Convective heat transfer boundaries were imposed between the covering materials (or floor) and the indoor air. The air supply inlet was set as a velocity inlet, with an air supply velocity of 6.0 m/s, a supply air temperature of 28° C, and a relative humidity of 78%. The corresponding water vapor mass fraction at the inlet was calculated as approximately 0.02, based on the psychrometric relationship at the specified temperature and relative humidity.

The return-air inlet was also set as a velocity inlet, but with a negative velocity (i.e., exhaust direction). Unlike conventional natural return or fixed-volume exhaust systems, the active return-air system adopted in this study allows independent regulation of the return air velocity according to the operational status of the heat pump exhaust fan. The return air velocity was calculated based on the supply air velocity, duct cross-sectional area, return inlet cross-sectional area, and return air ratio. The return inlet had a cross-sectional area of 0.35 m^2, and the return air ratio was set to 90% of the exhaust fan operating capacity, corresponding to a return air velocity of −2.0 m/s.

The room door was modeled as a wall boundary because doors remain closed during the fruiting stage to maintain a stable temperature and humidity. Forced ventilation was the dominant driver of indoor airflow, making any infiltration through the door negligible. This simplification is consistent with established CFD practices for controlled-environment facilities [13,19]. The cultivation substrate continuously releases metabolic heat during mushroom growth. Based on the ventilation heat balance calculation of the growing house, the volumetric heat source of the substrate was determined as 55 W/m^3. The

thermophysical properties of the substrate were calculated based on the measured moisture content and referenced to the relevant literature methods [13]: density of 387 kg/m^3, specific heat of 2908 J/(kg·K), and thermal conductivity of 0.134 W/(m·K).

A steady-state solution method was employed. The SIMPLEC algorithm was used for pressure–velocity coupling. For spatial discretization, the least-squares method was applied to the gradient term, whereas second-order upwind schemes were adopted for the momentum, energy, and turbulence kinetic energy equations to improve calculation accuracy. The residual convergence criterion was set to 10^{-6} for the energy equation and 10^{-3} for the momentum and turbulence transport equations. Each simulation case was iterated for 600 steps to reach convergence.

2.3. Parameter Design

Simulations were performed for a mushroom growing house equipped with a centrally suspended perforated duct and an active return-air system. In practice, duct-opening configurations are often determined empirically. In this study, the hole diameter and spacing were calculated based on the required supply airflow rate and jet decay relationship (see Sections 2.3.1 and 2.3.2), ensuring a consistent design basis across all scenarios.

Two rack-row configurations (two and three rows) were examined for the cultivation rack layout. To isolate the effect of row number on environmental uniformity, the total cultivation substrate volume was kept constant between configurations: the three-row layout adopted a narrower rack width of 0.7 m per row, while the two-row layout used a width of 1.0 m per row, maintaining the same total cultivation area across all schemes.

Regarding the supply angle design, *Volvariella volvacea* is known to be sensitive to direct airflow impingement on the canopy. Preliminary tests and the literature indicated that intermediate supply angles (between 0° and 90°) tend to direct airflow onto the canopy surface, which is detrimental to fruiting body development [11]. Therefore, only the horizontal (0°), vertical (90°), and their combination were selected for systematic comparison, resulting in the four scenarios summarized in Table 2: 2-0°, 2-90°, 2-0°+90°, and 3-0°.

Table 2. Design parameters for each simulation scenario.

Scenario	Number of Rack Rows	Outlet Direction	Hole Spacing (m)
2-0°	2	Horizontal 0° (3 and 9 o'clock)	0.66
2-90°	2	Vertical downward 90° (6 o'clock)	0.33
2-0°+90°	2	Combined: 6 o'clock + 3 and 9 o'clock	0.99
3-0°	3	Horizontal 0° (3 and 9 o'clock)	0.66

2.3.1. Supply Airflow Rate

During fruiting body development, straw mushrooms exhibit vigorous respiration with substantial CO_2 emission. When the indoor CO_2 concentration exceeds 1000 ppm, normal growth of fruiting bodies is inhibited. Mechanical ventilation is required to maintain acceptable indoor air quality and keep the CO_2 concentration within the permissible limit. The ventilation rate was determined based on the CO_2 mass balance equation: the amount of CO_2 released by mushroom respiration per unit time equals the difference between the CO_2 exhausted by the ventilation system and that introduced by the fresh air. The temporal

variation in the indoor CO_2 concentration can be described by the mass conservation differential equation [29]:

$$V_f \frac{dy}{dt} = G_{co_2} + Qy_0 - Qy \tag{7}$$

where V_f is the volume of the growing house (m^3), y is the indoor CO_2 mass concentration (g/m^3), G_{co_2} is the total CO_2 release rate from mushroom respiration (g/s), defined as $G_{co_2} = q_{co_2} A$, where q_{co_2} is the CO_2 emission rate per unit area ($g/(s \cdot m^2)$) and A is the total cultivation area (m^2), y is the mechanical ventilation rate (m^3/s), and y_0 is the CO_2 mass concentration in fresh air (g/m^3). Under steady operation of the ventilation system, when the indoor CO_2 concentration reaches equilibrium ($dy/dt = 0$), the minimum ventilation rate required to maintain the indoor CO_2 concentration below the allowable upper limit y_{max} is given by [30]:

$$Q_{min} = \frac{G_{co_2}}{y_{max} - y_0} \tag{8}$$

The unit of the right-hand side of Equation (8) is $(g/s)/(g/m^3) = m^3/s$, which is consistent with the unit of the left-hand side.

The permissible upper limit was set to 1000 ppm, and the fresh air CO_2 concentration was taken set to 400 ppm. The conversion between CO_2 volume concentration (ppm) and mass concentration (g/m^3) is given by:

$$y = C_{ppm} \times \frac{M_{co_2}}{V_m} \times \frac{273}{273 + T} \tag{9}$$

where C_{ppm} is the volume concentration (ppm), M_{co_2} = 44 g/mol is the molar mass of CO_2, V_m = 22.4 L/mol is the molar volume at standard conditions, and T is the room temperature (K), taken as 293.15 K (20 °C). Based on this conversion, 1 ppm corresponds to 0.00183 g/m^3.

Based on the field measurements of Zheng et al. [12], the CO_2 emission rate per unit area q_{co_2} was 0.00436 $g/(s \cdot m^2)$, and the total cultivation area A was 132 m^2. From $G_{co_2} = q_{co_2} A$, the total CO_2 release rate was calculated as G_{co_2} = 0.58 g/s. Substituting this value into Equation (8) gives = 0.51 m^3/s.

The total supply airflow rate of the perforated duct is given by the product of the average inlet velocity at the duct inlet and the duct cross-sectional area, which also equals the sum of the discharge rates through all supply holes:

$$Q = \frac{4\pi D^2}{V} \tag{10}$$

$$Q = \sum_{i=1}^{n} \left(C_{di} \frac{\pi D^2}{4} \sqrt{\frac{2P_i}{\rho}} \right) \tag{11}$$

The relationship between the fan inlet velocity and the airflow rate is expressed as:

$$V = \frac{4Q}{\pi D^2} \tag{12}$$

where D is the duct diameter, taken as 0.4 m. Substituting Q_{min} = 0.51 m^3/s into Equation (13), the minimum required fan inlet velocity was calculated as 4.04 m/s.

2.3.2. Duct Parameters

After the airflow is discharged from the supply holes, the jet velocity typically undergoes four stages of evolution: the near-field zone, where the jet velocity remains approximately equal to the outlet velocity; the initial diffusion zone, where the velocity begins to

decay in inverse proportion to the square root of the distance from the outlet; the intermediate diffusion zone, where the velocity is inversely proportional to the jet travel distance; and the far-field diffusion zone, where the velocity decays rapidly to the ambient airflow level. In the intermediate diffusion zone, the relationship between the jet centerline velocity and travel distance can be described by the following equation [31]:

$$x = \frac{V_i d K \sqrt{\pi C_{di}}}{2V_x} \tag{13}$$

where V_i is the air velocity at the supply hole (m/s), K is a constant (5.7) [31], C_{di} is the discharge coefficient of the supply hole (0.64), x is the distance from the supply hole (m), and V_x is the air velocity at distance x from the hole (m/s).

The air velocity V_i at the supply hole is a function of the static pressure P_i inside the duct, given by:

$$V_i = \sqrt{\frac{2P_i}{\rho}} \tag{14}$$

where ρ is the air density (kg/m^3), taken as 1.2 kg/m^3. It should be noted that Equation (14) gives the theoretical velocity based on Bernoulli's equation without considering the discharge coefficient. The actual discharge coefficient is then introduced in Equations (15) and (16) to account for the flow reduction caused by orifice geometry, following the approach of Wells et al. [31] Combining Equations (14) and (15), the supply hole diameter d can be expressed as:

$$d = \frac{xV_x}{K}\sqrt{\frac{2\rho}{\pi P_i C_{di}}} \tag{15}$$

According to the suitable airflow velocity range for the mushroom canopy (0.1–0.5 m/s) [32], the bottom cultivation layer (approximately 2.5 m from the supply holes) was selected as the design reference point. The expected jet centerline velocity at this location was set to V_x = 0.5 m/s, to ensure that the airflow retains sufficient momentum when reaching the bottom canopy layer, while avoiding excessive velocity that could damage the fruiting bodies. The static pressure at the duct inlet P_i was 30 Pa. Substituting the above parameters into Equation (16), the required supply hole diameter was calculated as d = 0.047 m. Considering manufacturing feasibility, the final supply hole diameter was set to 0.05 m (50 mm).

The number of supply holes per duct is determined by the ratio of total supply airflow rate to the flow rate through a single hole:

$$N = \frac{4Q}{C_{di}\pi d^2}\sqrt{\frac{\rho}{2P_i}} \tag{16}$$

where Q is the total supply airflow rate (m^3/s), taken as 0.51 m^3/s. Substituting the parameters, the number of supply holes was calculated as N $\approx$ 58.

The supply hole spacing L_d is determined by the duct length, total number of holes, and the number of hole rows:

$$L_d = \frac{L_b L}{N} \tag{17}$$

where L is the duct length (m), and L_b is the number of hole rows. Notably, N must be an exact integer multiple of L_b to ensure a symmetrical airflow distribution. In general, variable hole spacing is recommended for long ducts to maintain uniform discharge. However, the duct in this study is only 18.5 m long, and the measured temperature difference between

the inlet and the far end was about 0.2 °C. Therefore, a constant hole spacing was adopted for manufacturing simplicity, with negligible effect on air distribution uniformity.

To avoid direct airflow impingement on the mushroom canopy while ensuring adequate coverage of the cultivation zone, the duct was centrally suspended from the ceiling along the longitudinal direction. Figure 5 schematically illustrates the air supply directions and rack layouts of the four scenarios. Following the clock-face convention commonly used for flexible air distribution systems [33], horizontal supply is denoted as "3 and 9 o'clock" and vertical downward supply as "6 o'clock". The perforated duct had a diameter of 0.4 m and was fitted with 50-mm supply holes. The number of holes and the hole spacing for each scenario are listed in Table 2.

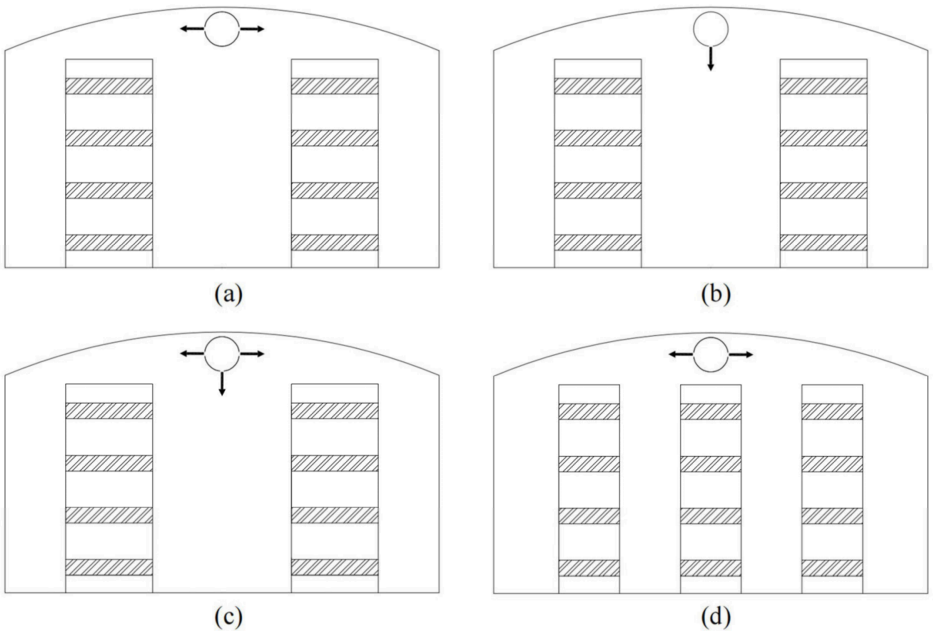


Figure 5. Schematic diagrams of the air supply directions and rack layouts for the four scenarios: (**a**) 2-0°; (**b**) 2-90°; (**c**) 2-0°+90°; (**d**) 3-0°.

2.3.3. Evaluation Methods

To evaluate the uniformity of airflow and temperature distributions across scenarios, variable coefficients were defined in both the horizontal (intra-layer) and vertical (inter-layer) directions. For each cultivation layer, a measurement plane was established 10 cm above the substrate surface, corresponding to the canopy height of the straw mushroom. Sixteen monitoring points were uniformly arranged on each plane at 1-m intervals along the layer length.

The horizontal coefficients of variation (CV) were used to evaluate the degree of dispersion of air velocity or temperature among different monitoring points within the same canopy layer, reflecting the horizontal uniformity of airflow distribution on that plane. The horizontal velocity CV $-$ V and horizontal temperature CV $-$ T for the k-th layer were defined as follows:

$$CV - V = \frac{\sqrt{\frac{1}{n-1}\sum_{i=1}^{n}\left(V_i - \overline{V}\right)^2}}{\overline{V}} \tag{18}$$

$$CV - T = \frac{\sqrt{\frac{1}{n-1}\sum_{i=1}^{n}\left(T_i - \overline{T}\right)^2}}{\overline{T}} \tag{19}$$

where n is the total number of monitoring points in the k-th layer; V_i is the air velocity at the i-th monitoring point of the k-th layer (m/s); $\overline{V}$ is the average velocity of the k-th layer

(m/s); T_i is the temperature at the i-th monitoring point of the k-th layer (°C); and $\overline{T}$ is the average temperature of the k-th layer (°C). Smaller values of $CV - V$ and $CV - T$ indicate better airflow and temperature uniformity.

The vertical CV was used to evaluate the degree of dispersion of the layer-average velocities or temperatures in the vertical direction, reflecting the environmental consistency among different cultivation layers. In this study, the vertical CV was calculated as the ratio of the standard deviation to the mean of the average velocities (or average temperatures) across the four layers. A smaller vertical CV indicates smaller environmental differences between layers and better vertical consistency.

In addition, the optimal zone area ratio was introduced as an indicator of airflow organization effectiveness [34]. Based on the optimal airflow velocity range for the straw mushroom canopy (0.1–0.5 m/s), each canopy layer section was divided into three zones: the optimal zone (0.1–0.5 m/s), the stagnant zone (<0.1 m/s), and the excessive-velocity zone (>0.5 m/s). The optimal zone area ratio was defined as the percentage of the area within the optimal velocity range relative to the total area of that layer. A higher ratio indicates a larger effective growing space for straw mushrooms under that scenario, corresponding to superior airflow organization performance.

2.3.4. AHP-Entropy-Weighted TOPSIS Evaluation Model

To provide a scientifically rigorous basis for ranking the four ventilation schemes, a multi-criteria decision-making (MCDM) framework combining the analytic hierarchy process (AHP), entropy weighting, and TOPSIS was adopted. Five evaluation indicators were selected based on a literature review and the physical requirements of multi-layer straw mushroom cultivation [11,21,34]: vertical velocity CV, horizontal (intra-layer) velocity CV, optimal-zone area ratio, excessive-velocity zone, and horizontal temperature CV. Vertical velocity CV reflects inter-layer airflow consistency and is the primary factor affecting yield uniformity across layers; optimal-zone area ratio directly represents the effective cultivation space; horizontal velocity CV characterizes intra-layer airflow uniformity; excessive-velocity zone indicates the risk of excessive airflow damage to fruiting bodies; and horizontal temperature CV reflects intra-layer thermal uniformity. The indicators were ranked in descending order of importance as: vertical velocity CV > optimal-zone area ratio > horizontal velocity CV > excessive-velocity zone > horizontal temperature CV.

The AHP method was first applied to determine the subjective weights. A pairwise comparison matrix was constructed using the 1–9 scale, and the consistency ratio (CR) was calculated to verify the logical consistency of the judgments. With CR = 0.023 < 0.1, the subjective weight vector w_{hj} = (0.298, 0.263, 0.201, 0.161, 0.077) corresponding to vertical velocity CV, optimal-zone area ratio, horizontal velocity CV, excessive-velocity-zone area ratio, and horizontal temperature CV, respectively [35].

Subsequently, the entropy weight method was employed to determine objective weights based on the inherent dispersion of the indicator data. Indicators with greater variability across schemes were assigned higher weights, reflecting their greater contribution to distinguishing scheme performance. The objective weight vector w_{ej} was then combined with the subjective weights w_{hj} using the multiplicative normalization method to obtain the combined weight w_{cj} for each indicator [36]:

$$w_{\mathrm{cj}} = \frac{w_{ej} \cdot w_{hj}}{\sum_{j=1}^{n} w_{ej} \cdot w_{hj}}, j = 1, 2, \ldots, n \tag{20}$$

where w_{hj} and w_{ej} denote the subjective and objective weights of the j-th indicator, respectively. This combined weighting approach integrates expert knowledge with data-driven information, thereby reducing the bias inherent in either weighting method alone.

Finally, the TOPSIS method was applied to rank the four schemes [35]. A weighted normalized decision matrix was constructed, and the positive and negative ideal solutions were determined. The Euclidean distances from each scheme to both the positive and negative ideal solutions were calculated, and the relative closeness coefficient was derived for each scheme. Schemes with higher closeness coefficients were considered to exhibit better overall performance across the five evaluation indicators.

3. Results and Discussion

3.1. Model Validation

To ensure the reliability of the CFD model for subsequent comparative analyses of different scenarios, the simulation results were validated against field measurements. Figure 6a compares the simulated and measured values of the in-duct air velocity at each measuring point along the duct and the outlet velocity at the supply holes. Along the airflow direction, the in-duct velocity gradually decreased from approximately 6.0 m/s at the inlet to near zero at the end, due to wall friction and outflow dissipation. The simulated values followed the same trend as the measured values, with absolute deviations ranging from 0.01 to 0.35 m/s. The mean relative errors were 7.2% for the in-duct velocity and 9.5% for the outlet velocity at the supply holes.

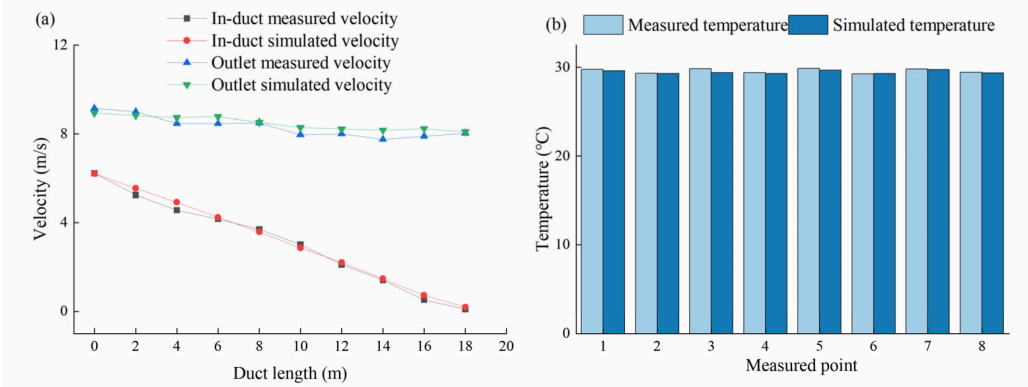


Figure 6. Comparison between simulated and measured values: (**a**) in-duct air velocity and outlet velocity at supply holes; (**b**) temperature at different monitoring points.

Figure 6b shows the simulated and measured temperatures at the mushroom canopy layer for each monitoring point inside the growing house. A distinct vertical temperature gradient was observed, with temperatures gradually increasing from the lower to the upper layers. The absolute deviations between the simulated and measured values ranged from 0.1 to 0.4 °C, with a mean relative error of 1.1%. The CFD model was validated against field measurements with acceptable errors for both velocity and temperature, confirming its suitability for subsequent scenario analyses.

3.2. Velocity Field

Figures 7 and 8 present the velocity contours and streamline vectors, respectively, on a typical longitudinal section (X = 9.5 m) of the growing house under the four scenarios. Overall, the air velocity in the cultivation zone was predominantly below 0.5 m/s under all scenarios, falling within the suitable range for straw mushroom growth (0.1–0.5 m/s). Localized excessive-velocity zones were confined to the jet core region and at local vortex centers.

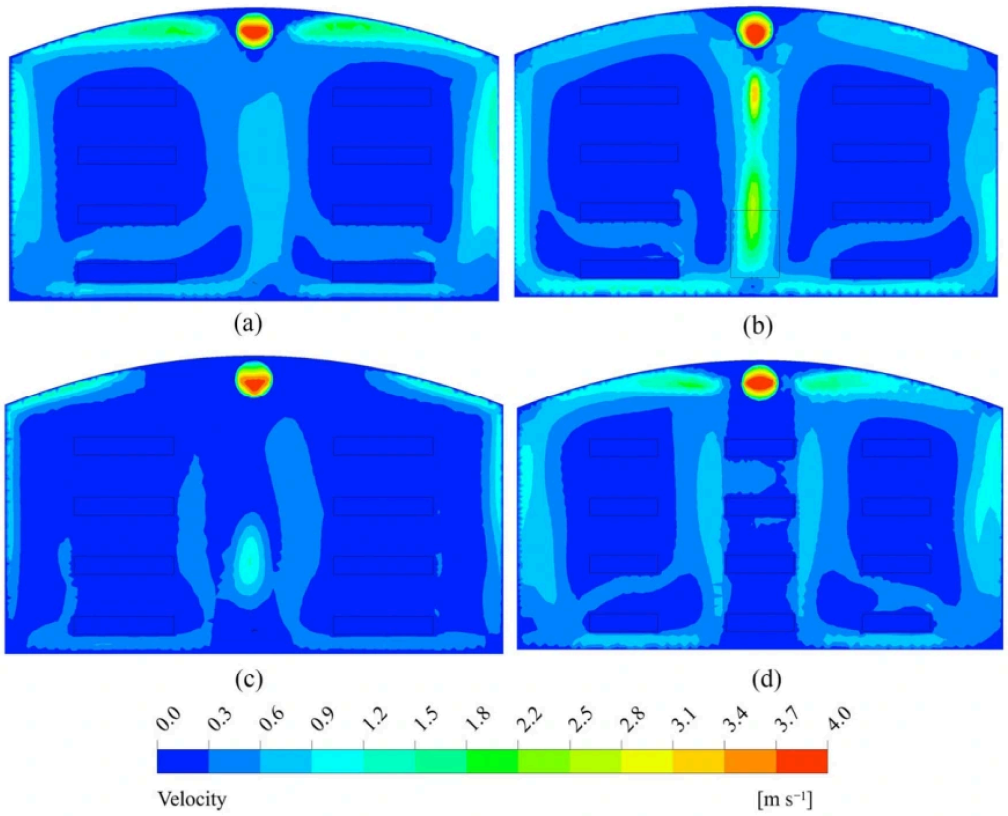


Figure 7. Velocity contours on the longitudinal section at X = 9.5 m under different scenarios: (**a**) 2−0°; (**b**) 2−90°; (**c**) 2−0°+90°; (**d**) 3−0°.

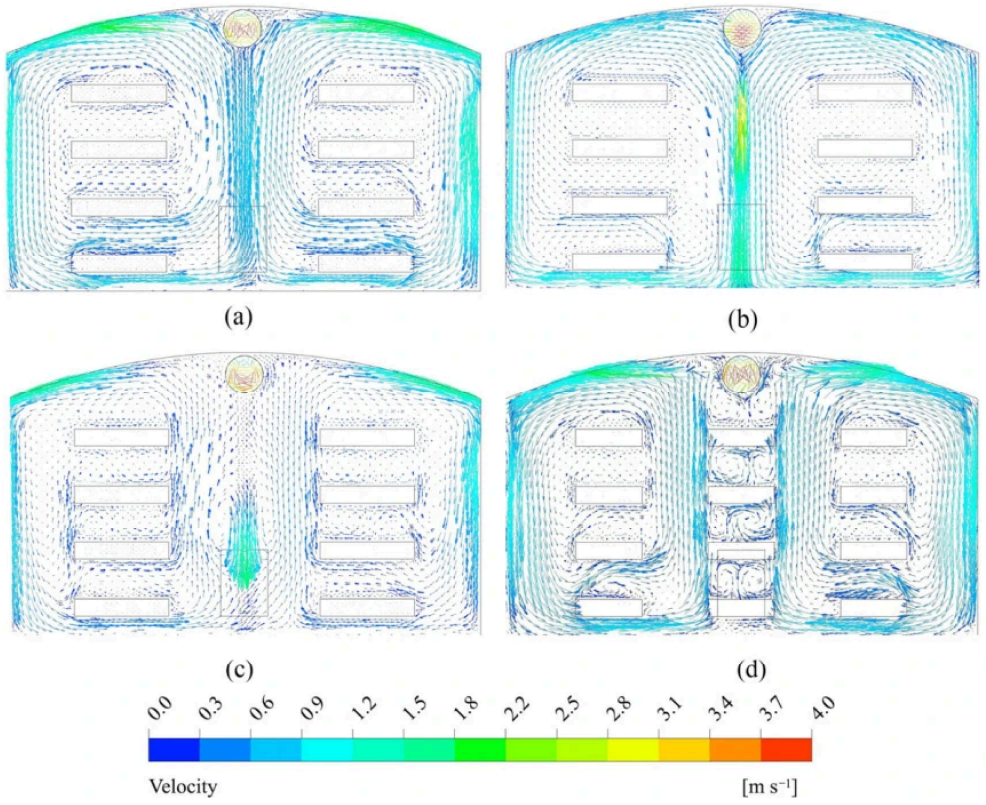


Figure 8. Streamline vectors on the longitudinal section at X = 9.5 m under different scenarios: (**a**) 2−0°; (**b**) 2−90°; (**c**) 2−0°+90°; (**d**) 3−0°.

The horizontal supply scenarios (2-0° and 3-0°) exhibited a pronounced wall attachment effect: the jets attached to the sidewalls, turned downward, spread along the floor and the top surface of the bottom cultivation layer toward the central aisle, where they converged and rose upward. Unlike 2-0°, which formed two symmetrical counter-rotating recirculation loops, 3-0° generated upward flow in two adjacent aisles due to the addition of a third rack row. This formed a double-vortex structure, which increased flow complexity but resulted in more dispersed vortex intensity in the intermediate region. This indicates that increasing the number of rack rows not only alters aisle width but fundamentally reconstructs the jet trajectory and vortex topology.

In the vertical supply scenario (2-90°), the jet impinged vertically on the floor and spread horizontally to both sides, resulting in a relatively high air velocity near the bottom layer. Meanwhile, local turbulent vortices were induced between the first and second cultivation layers, which facilitated thermal boundary layer breakup and promoted inter-layer air and CO_2 mixing [19]. In the combined scenario (2-0°+90°), the horizontal wall-attached jet and the vertical impinging jet superimposed on each other. The vector diagram showed a strong concentrated vortex in the central aisle, with notably higher velocities near the aisle-side regions of the cultivation racks, while the velocities within the canopy zones themselves remained at relatively low levels.

A comparison of the three jet configurations reveals distinct flow behaviors. The vertical supply delivered momentum downward along the shortest diffusion path, resulting in more uniform bottom-layer coverage. The horizontal supply experienced long-distance momentum attenuation along the walls, tending to form localized stagnant zones within the large-scale circulation. The combined scenario, although incorporating both flow characteristics, concentrated the momentum primarily in the aisle region, with relatively limited direct influence on the canopy space inside the racks.

Figure 9 presents the velocity contours and vectors on the first and fourth canopy sections under the four scenarios. The full set of four-layer canopy velocity distributions is provided in the Supplementary Materials. Horizontally, all scenarios exhibited a consistent distribution pattern: higher velocities near the aisles and lower velocities inside the rack interiors, with the excessive-velocity zones primarily distributed along both sides of the aisles, indicating a significant blocking effect of the cultivation racks on airflow penetration. The vector plots further reveal distinct flow characteristics across scenarios. In the horizontal supply scenarios (2-0° and 3-0°), large-scale recirculation vortices formed in the aisles, with airflow predominantly horizontal and vertical perturbation relatively weak. In contrast, the 2-90° vertical supply scenario produced a pronounced downward-penetrating flow, with vectors radiating from the aisles toward both sides within the canopy region, indicating substantially enhanced vertical perturbation. The combined scenario (2-0°+90°) exhibited intermediate behavior between the two.

Figure 10 presents the layer-average velocities and coefficients of variation (CV) for each scenario. Within a canopy layer, the horizontal CV quantifies the uniformity, while the vertical CV reflects the consistency across the four layers. Among the scenarios, the horizontal supply scenarios (2-0° and 3-0°) generally exhibited higher average velocities across all canopy layers than those with a vertical component. In 2-0°, the first-layer average velocity reached 0.50 m/s (the highest among all scenarios), with the horizontal CV increasing from 24.0% to 32.5% with layer height, indicating an intensifying gradient between the near-wall excessive-velocity zone and the inner-rack stagnant zone. In contrast, 2-90° exhibited the closest layer-average velocities (0.21–0.25 m/s), with a vertical CV of only 8.7%, which is the lowest among all scenarios and confirms its optimal inter-layer consistency. However, its horizontal CV (29.2–53.4%) was slightly higher than that of 2-0°, indicating a substantial transverse gradient between the aisles and the deeper rack zones

during horizontal spread. In other words, the advantage of vertical supply lies in vertical consistency rather than horizontal uniformity.

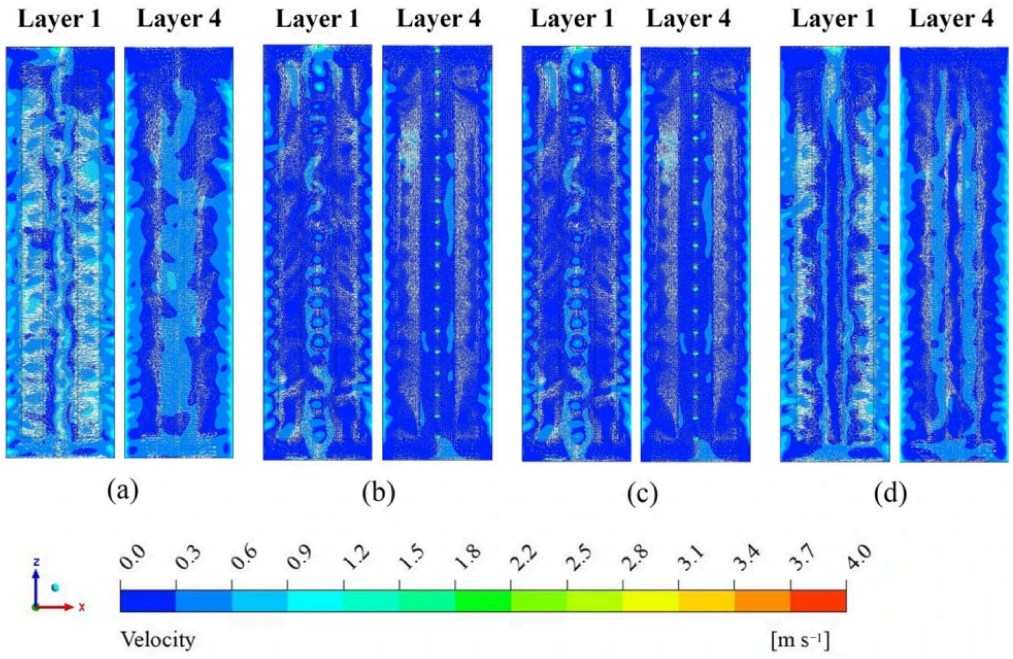


Figure 9. Velocity contours on canopy sections (10 cm above the substrate) across four cultivation layers: (**a**) 2−0°; (**b**) 2−90°; (**c**) 2−0°+90°; (**d**) 3−0°.

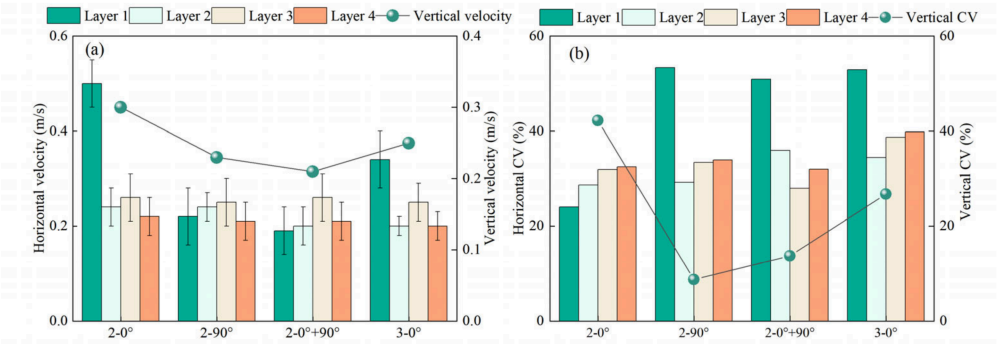


Figure 10. Statistical analysis of canopy-layer velocity: (**a**) layer-average velocity (bars: horizontal velocity; line: vertical velocity); (**b**) coefficients of variation (bars: horizontal CV; line: vertical CV).

The 3-0° scenario had a vertical CV (26.7%) between that of 2-0° (42.2%) and 2-0°+90° (13.7%), indicating that the third rack row diverted jet momentum and partially mitigated inter-layer differences. The 2-0°+90° scenario had the second-lowest vertical CV, and its horizontal CV exhibited relatively little fluctuation across layers (27.9–50.9%), suggesting that introducing a vertical momentum component contributed to improvements in both vertical consistency and horizontal uniformity.

As shown in Figure 11, the mean optimal zone area ratio directly reflects the effective growing space and serves as a core indicator of airflow organization effectiveness. The stagnant zone (<0.1 m/s) area ratios showed limited variation across scenarios (5–15%). For the excessive-velocity zone (>0.5 m/s), marked differences were observed: the first-layer ratio reached 48.9% in 2-0°, 20.8% in 3-0°, while 2-90° maintained below 1% across all layers. For the optimal-zone area ratio, 2-90° achieved approximately 90% across all layers (85.1–94.4%), with minimal vertical variation (CV = 2.8%). The 2-0°+90° scenario had a

slightly higher average (90.7%) but larger vertical fluctuation (CV = 6.7%), whereas 2-0° (81.5%) and 3-0° (87.1%) were lower.

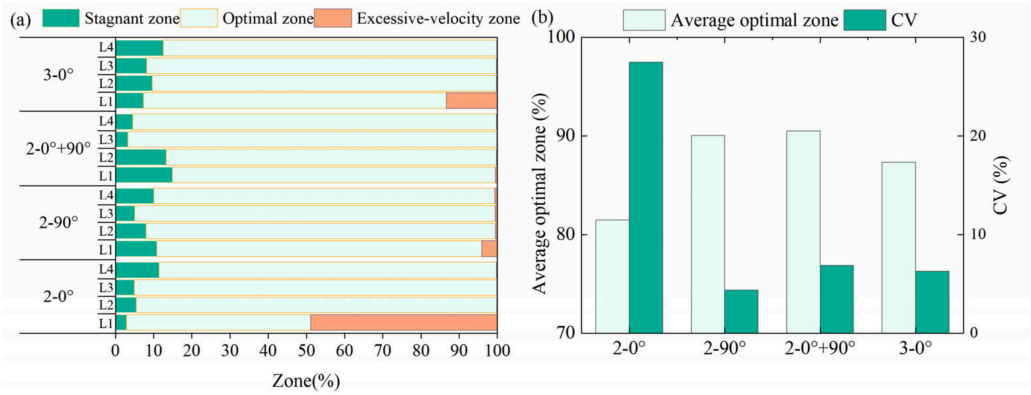


Figure 11. Velocity zoning analysis of canopy layers under different scenarios: (**a**) zone area ratios by layer; (**b**) mean optimal zone area ratio and inter-layer CV.

Overall, schemes with a vertical component outperformed purely horizontal ones, with 2-90° achieving the most stable performance due to its lowest vertical CV. Using the optimized side-supply case of Peng et al. [11] as a benchmark, which yielded a velocity non-uniformity coefficient of 46.1%, the present 2-0° and 2-90° schemes achieved vertical CVs of 42.2% and 8.7%, respectively. This marked improvement, however, arises from a fundamentally different configuration. In side-wall diffuser systems with wall-reflected jets, intermediate angles (30–60°) are typically favored, as purely horizontal discharge suffers from boundary adhesion and momentum decay, while vertical discharge from ceiling diffusers may produce overly concentrated impingement [17,18]. The centrally suspended duct and lower return inlet deliver the 90° jet directly downward along the shortest geometric route, with the floor acting as the distribution surface. This mechanism explains the superior vertical uniformity of the 2-90° scheme, which achieved a vertical velocity CV of 8.7% compared to 42.2% (2-0°) and 26.7% (3-0°). The comparison between 2-0° and 3-0° further reveals that increasing rack rows alters the global circulation structure rather than merely adjusting aisle width, supporting the view that rack geometry functions as an active flow-guiding element rather than a passive obstruction [19,20].

3.3. Temperature Field

Figure 12 presents the temperature contours on a typical longitudinal section (X = 9.5 m) under the four scenarios. The temperature ranged from 28.4 °C to 30.3 °C across all scenarios, with a pronounced vertical stratification: higher temperatures in the upper rack region (>29.5 °C) and lower temperatures in the lower region (<28.8 °C). Among the scenarios, 2-0° exhibited the weakest vertical temperature stratification, indicating the best inter-layer temperature uniformity. The 2-0°+90° scenario fell between the vertical and horizontal modes, with its vertical momentum component partially mitigating heat accumulation in the upper layers.

Figure 13 presents the temperature contours of the first and fourth canopy sections under the four scenarios, with the full four-layer dataset provided in the Supplementary Materials. Consistent with the sectional contours in Figure 11, the canopy temperatures across all scenarios ranged from 28.4 °C to 30.3 °C. Vertically, temperature stratification remained observable at the canopy scale, although the inter-layer differences were smaller than those in the overall sectional distribution. Horizontally, all scenarios exhibited higher temperatures near the return-air inlet and lower temperatures farther away; this was associated with the circulation of the heat-carrying return airflow, consistent with the findings of Jing

et al. [14]. Notably, the 3-0° scenario exhibited the smallest high-temperature zone area and the most uniform horizontal temperature distribution, indicating that the three-row rack layout dispersed the heat sources more effectively in the horizontal direction, alleviating localized heat accumulation and improving canopy-scale temperature uniformity.

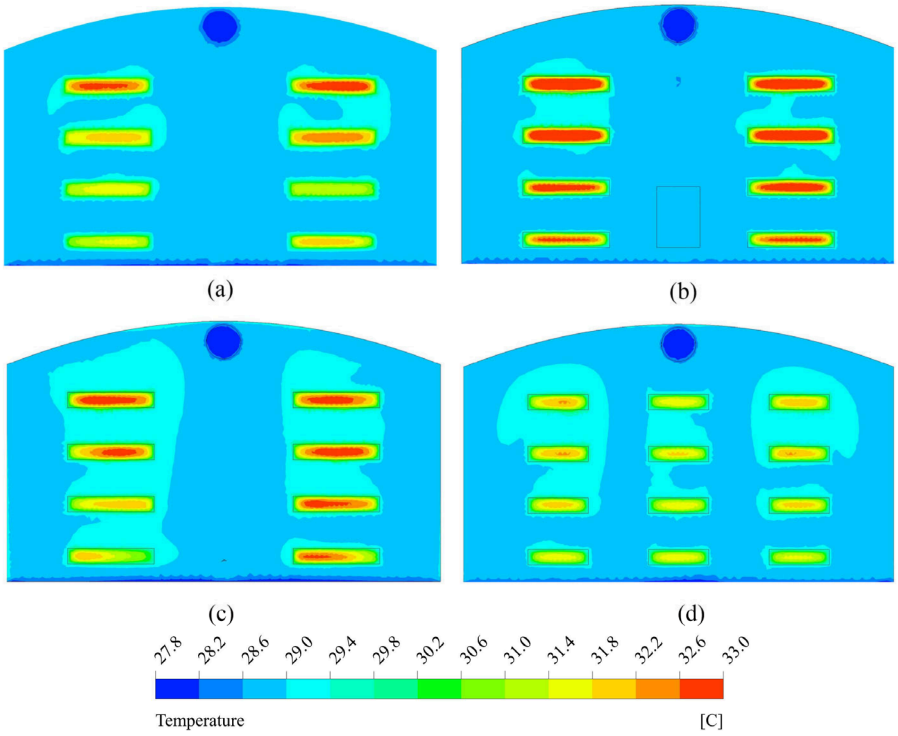


Figure 12. Temperature contours on the longitudinal section at X = 9.5 m under different scenarios: (**a**) 2−0°; (**b**) 2−90°; (**c**) 2−0°+90°; (**d**) 3−0°.

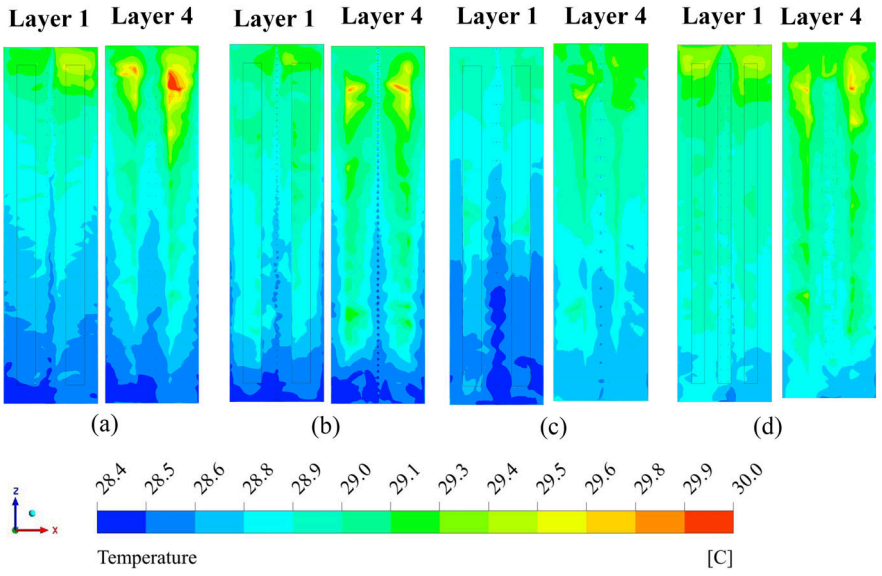


Figure 13. Temperature contours on canopy sections (10 cm above the substrate) across four cultivation layers: (**a**) 2-0°; (**b**) 2-90°; (**c**) 2-0°+90°; (**d**) 3-0°.

The statistical results for layer-average temperatures and coefficients of variation are shown in Figure 14. Inter-layer temperature differences were small across all scenarios (maximum <0.3 °C). In terms of vertical temperature uniformity, 2-0° exhibited the lowest vertical CV (0.16%), followed by 3-0° (0.19%), 2-0°+90° (0.21%), and 2-90° (0.22%). For horizontal temperature uniformity, 3-0° showed the lowest horizontal CV across all layers

(0.26–0.49%), attributable to the three-row rack layout dispersing heat sources more effectively. The other scenarios ranked as: 2-0° (0.43–0.59%), 2-90° (0.42–0.58%), and 2-0°+90° (0.52–0.57%), though differences were minor. Overall, the temperature field was substantially more uniform than the velocity field, and its sensitivity to supply parameters was considerably lower.

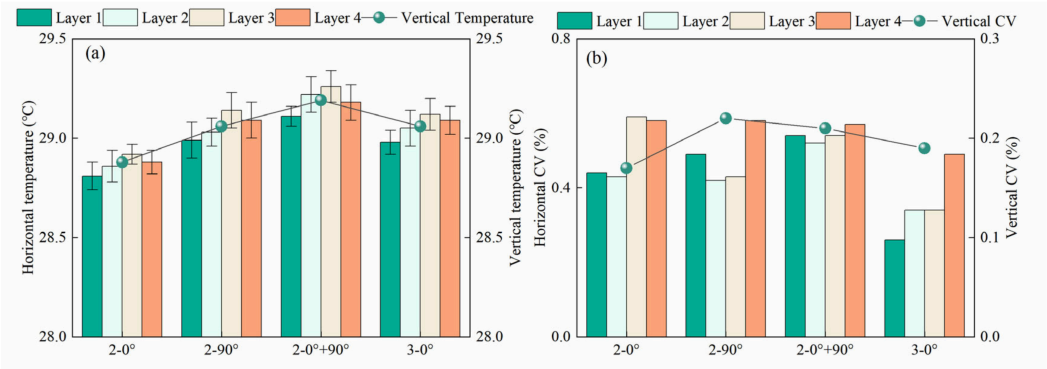


Figure 14. Statistical analysis of canopy-layer temperature: (**a**) layer-average temperature (bars: horizontal temperature; line: vertical temperature); (**b**) horizontal and vertical coefficients of variation (bars: horizontal CV; line: vertical CV).

3.4. Comprehensive Evaluation

To overcome the limitations of single-indicator assessments, the AHP-entropy-weighted TOPSIS model was employed to comprehensively rank the four ventilation schemes. The evaluation system comprised five indicators: optimal-zone area ratio, excessive-velocity zone area ratio, vertical velocity CV, horizontal (intra-layer) velocity CV, and horizontal temperature CV. Among these, the optimal-zone area ratio was treated as a positive indicator (higher is better), while the remaining four were treated as negative indicators (lower is better). Subjective weights were determined based on the physical requirements of straw mushroom cultivation (CR = 0.023 < 0.1), and objective weights were derived using the entropy method. The combined weights were obtained via multiplicative normalization (Table 3).

Table 3. Weight allocation for the five evaluation indicators.

Indicator	Subjective Weight	Objective Weight	Combined Weight
optimal-zone area ratio	0.154	0.263	0.217
excessive-velocity zone area ratio	0.147	0.161	0.127
vertical velocity CV	0.167	0.298	0.267
horizontal velocity CV	0.256	0.201	0.276
horizontal temperature CV	0.277	0.077	0.114

Based on the combined weights, the TOPSIS method was applied to calculate the relative closeness coefficient for each scheme. The ranking of the four schemes, in descending order of overall performance, was: 2-90° (0.616) > 2-0°+90° (0.604) > 3-0° (0.423) > 2-0° (0.417). After normalization of the five indicators, the radar chart (Figure 15) visually compares the multi-dimensional performance of each scheme. The 2-90° scheme exhibits the most balanced profile, with outstanding performance in the vertical velocity CV and the optimal-zone area ratio, which effectively compensates for its moderate performance in the horizontal velocity CV. The 2-0°+90° scheme achieves near-maximum scores in excessive-velocity zone and optimal-zone area ratio, yet its vertical velocity CV score is relatively low, resulting in a noticeable concavity in its radar profile. In contrast, the purely horizontal supply

schemes (2-0° and 3-0°) show markedly skewed radar profiles, with substantially lower overall coverage than the schemes incorporating a vertical component; among them, 2-0° performs the poorest across all dimensions, with the lowest closeness coefficient. The two schemes with a vertical component achieved significantly higher closeness coefficients than the purely horizontal schemes, confirming that introducing a vertical momentum component plays a decisive role in improving environmental uniformity in multilayer mushroom cultivation.

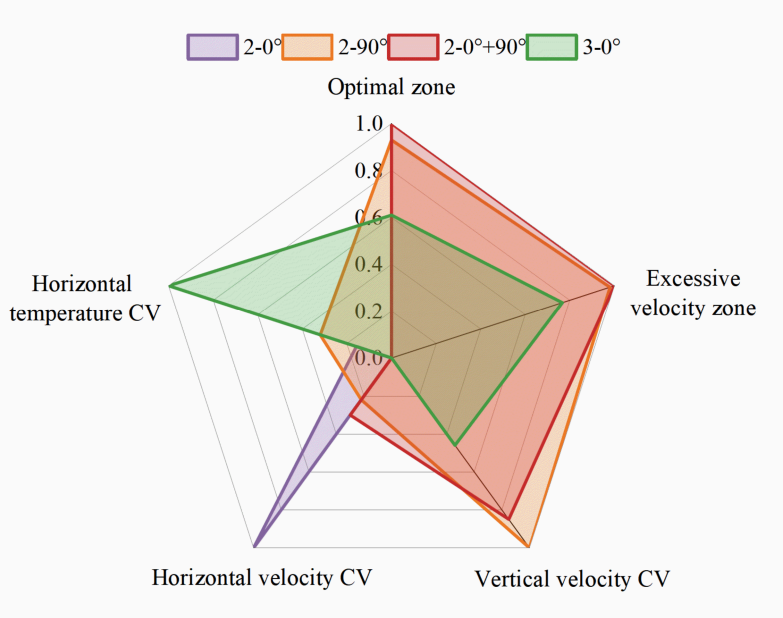


Figure 15. Radar chart of the normalized multi-indicator performance for the four ventilation schemes.

4. Conclusions

To our knowledge, this study provides the first systematic quantification of the coupled effects of the air supply angle and cultivation rack row number on environmental uniformity in an active return-air mushroom growing house. Our results, supported by good agreement between the CFD simulations and field measurements, demonstrate that the air supply angle and the cultivation rack row number do not act independently: their interaction is configuration-dependent, and the optimal arrangement differs between velocity and temperature uniformity. The key findings are summarized as follows:

The coupled analysis revealed that the supply angle and rack row number significantly interact. Vertical downward supply combined with a two-row layout (2-90°) achieved the best overall performance, with a vertical velocity CV of 8.7% and a mean optimal-zone area ratio of approximately 90%. This superiority is explained by three interrelated physical mechanisms: the direct downward jet follows the shortest path to the floor, minimizing turbulent momentum decay before lateral deflection; the vertical momentum drives airflow through all cultivation layers, suppressing stratification; and impingement on the floor induces lateral deflection and inter-layer mixing. In contrast, the horizontal supply scenarios exhibited strong wall-attachment effects, whereas the mixed-angle scheme showed intermediate performance, indicating that horizontal components disrupt the vertical jet without additive benefits. Notably, the optimal configuration differs between the velocity and temperature fields: whereas vertical downward supply with two rows excels in velocity uniformity, horizontal supply with three rows offers superior horizontal temperature uniformity by dispersing the heat sources more evenly. This trade-off underscores the value of a multi-criteria evaluation. An AHP-entropy-weighted TOPSIS assessment integrating five

indicators across the velocity and temperature fields confirmed that schemes incorporating a vertical component consistently outperformed the horizontal ones. The 2-90°scheme ranked highest, followed by 2-0°+90°.

For the 5-m-wide mushroom house investigated in this study, the following design parameters are recommended: supply outlet velocity of 6.0 m/s; duct suspension height of 2.3–2.7 m above the floor; two-row rack layout with a central aisle of 1.5–1.8 m; and vertical downward (90°) supply orientation. These recommendations are based on the present active return-air system with a centrally suspended duct. Generalization to conventional side-wall supply layouts requires further validation. In addition, the present steady-state approach does not account for transient effects during rapid environmental changes. Future work may further investigate the effects of intermediate supply angles (e.g., 15–45°), supply air velocity, and return air velocity on environmental uniformity under the optimal configuration identified in this study, so as to determine the optimal operating parameters for the straw mushroom canopy.

Supplementary Materials: The following supporting information can be downloaded at: https://www.mdpi.com/article/10.3390/agriculture16202263/s1. Supplementary Figure S1: Photographs of the experimental facility and measurement setup.

Author Contributions: Conceptualization, S.L. and C.W. (Chuanqing Wang); methodology, S.L., C.W. (Chuanqing Wang), and C.W. (Chunhui Wang); software, C.W. (Chuanqing Wang); validation, C.W. (Chuanqing Wang) and C.W. (Chunhui Wang); formal analysis, C.W. (Chuanqing Wang); investigation, C.W. (Chuanqing Wang), X.D., C.W. (Chunhui Wang), G.Z., Y.C. and X.X.; resources, S.L., X.D., G.Z., Y.C. and X.X.; data curation, C.W. (Chuanqing Wang); writing—original draft preparation, C.W. (Chuanqing Wang); writing—review and editing, S.L., C.W. (Chuanqing Wang) and C.W. (Chunhui Wang); visualization, C.W. (Chuanqing Wang); supervision, S.L., X.D., G.Z., Y.C. and X.X.; project administration, S.L.; funding acquisition, S.L. All authors have read and agreed to the published version of the manuscript.

Funding: This research was funded by the National Key R&D Plan of China Program: Development and Application of Intelligent Equipment for Edible Fungi Production (Grant No. 2024YFD2000702).

Data Availability Statement: The original contributions presented in this study are included in the article. Further inquiries can be directed to the corresponding author.

Conflicts of Interest: Author Xijia Xu was employed by the company Shaoguan Starway Bio-Technology Co., Ltd. Yuefeng Chen was employed by the company Zhejiang Branch of Chinese Academy of Agricultural Mechanization Sciences Group Co., Ltd. The remaining authors declare that the research was conducted in the absence of any commercial or financial relationships that could be construed as a potential conflict of interest.

Nomenclature

A	Total cultivation area, m^2	R_i	Net rate of production by chemical reaction, $kg/(m^3 \cdot s)$
a	Area of a hole, m^2	S	Source term
C	Overall discharge coefficient	S_{ct}	Turbulent Schmidt number
C_2	Inertial resistance coefficient, m^{-1}	S_i	User-defined source term for species, $kg/(m^3 \cdot s)$
C_d	Discharge coefficient	S_ϕ	Source term in general equation
C_{di}	Discharge coefficient of a hole	T	Temperature, K or °C
C_p	Specific heat capacity of air, J/(kg·K)	T_i	Temperature at i-th point, °C
C_{ppm}	CO_2 volume concentration, ppm	$\overline{T}$	Average temperature of a layer, °C
CV	Coefficient of variation	u_i	Velocity component in i-direction, m/s
$CV-T$	Horizontal temperature CV	V	Average velocity at duct inlet, m/s
$CV-V$	Horizontal velocity CV	V_f	Volume of the growing house, m^3
D	Duct diameter, m	V_i	Air velocity at i-th point, m/s
d	Hole diameter, m	V_m	Molar volume at standard conditions, L/mol

d_p	Effective particle diameter, m	V_x	Air velocity at distance x, m/s
$D_{i,m}$	Diffusion coefficient of species i, m^2/s	W_{hj}	Subjective weight
G_{co_2}	Total CO_2 release rate, g/s	W_{ej}	Objective weight
J_i	Diffusion flux of species i, kg/(m^2·s)	x	Distance from supply hole, m
K	Constant in jet equation	Y_i	Mass fraction of species i
k	Turbulent kinetic energy, m^2/s^2	y	Indoor CO_2 mass concentration, g/m^3
L	Duct length, m	y_0	CO_2 concentration in fresh air, g/m^3
L_b	Number of hole rows	y_{max}	Allowable upper limit, g/m^3
L_d	Supply hole spacing, m	α	Permeability, m^2
M_{co_2}	Molar mass of CO_2, g/mol	Γ	Generalized diffusion coefficient
N	Number of supply holes	Γ_ϕ	Diffusion coefficient for φ
n	Number of monitoring points	γ	Substrate porosity
P	Pressure, Pa	ε	Turbulent dissipation rate, m^2/s^3
P_i	Static pressure inside the duct, Pa	μ	Dynamic viscosity of air, Pa·s
Q	Mechanical ventilation rate, m^3/s	μ_t	Turbulent viscosity, Pa·s
Q_{min}	Minimum ventilation rate, m^3/s	ρ	Air density, kg/m^3
q_{co_2}	CO_2 emission rate per unit area, g/(s·m^2)	ϕ	Generalized variable

References

1. Wang, M.Y.; Zhou, D.H.; Wang, D.; Zhao, X.P.; Ren, C.H.; Song, W.D. Current status and prospects of edible fungi production equipment at home and abroad. *Acta Edulis Fungi* **2026**, *33*, 107–115. [CrossRef]
2. Ren, C.H.; Wang, M.Y.; Wu, J.J.; Zhou, F.; Zhou, D.H.; Chen, B. Research status and prospect of edible fungus factory equipment in China. *J. Chin. Agric. Mech.* **2025**, *46*, 207–213. [CrossRef]
3. Chen, L.; Qian, L.; Zhang, X.; Li, J.Z.; Zhang, Z.J.; Chen, X.M. Research progress on indoor environment of mushroom factory. *Int. J. Agric. Biol. Eng.* **2022**, *15*, 25–32. [CrossRef]
4. Gao, J.L.; Xiong, Y.J.; Sun, S.Q.; Xu, R.L.; Liu, Y.H. Establishment and simulation study of temperature and airflow distribution models for industrialized mushroom production. *J. Jiangsu Agric. Sci.* **2018**, *46*, 242–247. [CrossRef]
5. Islam, M.T.; Zakaria, Z.; Hamidin, N.; Mohd Ishak, M.A.B. A competitive study on higher yield performance in indoor optimized environment and outdoor cultivation of Pleurotus pulmonarius. *MAYFEB J. Agric. Sci.* **2016**, *2*, 13–27.
6. Qin, H.J.; Chen, P.; Wang, Q.; Zhang, J. The chemical composition, biological activity and cultivation situation of straw mushroom. *Food Ind.* **2017**, *38*, 203–206.
7. Liu, Y.J.; Zhang, L.N.; Chen, Y.F.; Lv, H.Z.; Guo, Y.L.; Ding, W.; Wang, T.Y. Research progress on industrialized production technology for straw mushroom. *Agric. Eng.* **2026**, *16*, 40–47. [CrossRef]
8. Nwankwegu, A.S.; Hongsanan, S.; Nwankwegu, U.P.; Xie, N. Exploring the critical environmental optima and biotechnological prospects of fungal fruiting bodies. *Microb. Biotechnol.* **2025**, *18*, e70210. [CrossRef]
9. Zhou, C.F.; Zong, W.Y.; Yang, F.; Tan, F. Numerical simulation and analysis of the ventilation process of a plastic greenhouse air bag system. *J. Gansu Agric. Univ.* **2023**, *58*, 269–278. [CrossRef]
10. Han, J.H.; Kwon, H.J.; Yoon, J.Y.; Kim, K.; Nam, S.W.; Son, J.E. Analysis of the thermal environment in a mushroom house using sensible heat balance and 3-D computational fluid dynamics. *Biosyst. Eng.* **2009**, *104*, 417–424. [CrossRef]
11. Peng, W.H.; Li, J.; Zheng, Q.H. Research into the characteristics of delivering air distribution to north straw mushroom plant in winter. *Shanxi Archit.* **2007**, *33*, 2. [CrossRef]
12. Zheng, Q.H.; Wang, L. The program of natural ventilation for Volariella volacea workshop in spring and autumn in northern regions. *Build. Energy Environ.* **2008**, *27*, 80–82. [CrossRef]
13. Cheng, Y.H.; Wang, X.Z.; Wu, Y.X.; Yang, H.P. Study on CFD simulation of edible mushroom house environment and air supply pipe layout scheme. *J. Agric. Mech. Res.* **2022**, *44*, 16–21. [CrossRef]
14. Jing, L.; Shen, M. CFD simulation and verification of flow and temperature fields in mushroom house. *J. Chin. Agric. Mech.* **2016**, *37*, 84–88. [CrossRef]
15. Wei, Z.B.; Jin, Z.J.; Chen, Q.; Zong, T.X. Research and development of an intelligent environmental control system for mushroom room of Flammulina velutipes. *Agric. Eng.* **2025**, *15*, 63–68. [CrossRef]
16. Wang, T.X.; Lai, H.G.; Wang, T. Optimization research on internal environment of seafood mushroom cultivation house based on CFD. In Proceedings of the 16th Annual China CAE Engineering Analysis Technology Conference, Deqing, China, 24–25 October 2020; p. 6.
17. Jiao, L.Z.; Duan, X.S.; Shao, B.; Liu, L.; Liu, D.H. The influence of different orifice angles of flexible air duct on the shelf placement in pharmaceutical warehouse. *Build. Energy Effic.* **2023**, *51*, 42–47. [CrossRef]

18. Hou, F.L.; Shen, C.H.; Cheng, Q. Research on a new optimization method for airflow organization in breeding air conditioning with perforated ceiling ventilation. *Energy* **2022**, *254*, 124279. [CrossRef]
19. Lee, S.H.; Yu, B.K.; Lee, C.J.; Lim, Y.T. The study on enhanced micro climate of the oyster mushroom cultivation house with multi-layered shelves by using CFD analysis. *J. Mushrooms* **2017**, *10*, 14–20. [CrossRef]
20. Li, Y.M.; Sun, F.J.; Shi, W.B.; Liu, X.G.; Li, T.L. Numerical simulation of ventilation performance in mushroom solar greenhouse design. *Energies* **2022**, *15*, 5899. [CrossRef]
21. Lim, T.-G.; Kim, Y.H. Analysis of airflow pattern in plant factory with different inlet and outlet locations using computational fluid dynamics. *J. Biosyst. Eng.* **2014**, *39*, 310–317. [CrossRef]
22. Bao, E.C.; Zou, Z.R.; Zhang, Y. CFD simulation of heat transfer in back-wall of active thermal-storage solar greenhouse with different airflow directions. *Trans. Chin. Soc. Agric. Eng.* **2018**, *34*, 169–177. [CrossRef]
23. He, X.J.; Wang, J.; Guo, S.R.; Zhang, J.; Wei, B.; Sun, J.; Shu, S. Ventilation optimization of solar greenhouse with removable back walls based on CFD. *Comput. Electron. Agric.* **2018**, *149*, 16–25. [CrossRef]
24. Liu, M.Y.; Jiang, C.; Khoo, B.C.; Zhu, H.F.; Gao, G.G. A cell-based smoothed finite element model for the analysis of turbulent flow using realizable k-ε model and mixed meshes. *J. Comput. Phys.* **2024**, *501*, 112783. [CrossRef]
25. Posner, J.D.; Buchanan, C.R.; Dunn-Rankin, D. Measurement and prediction of indoor air flow in a model room. *Energy Build.* **2003**, *35*, 515–526. [CrossRef]
26. Shih, T.H.; Liou, W.W.; Shabbir, A.; Yang, Z.; Zhu, J. A new k-ε eddy viscosity model for high Reynolds number turbulent flows–model development and validation. *Comput. Fluids* **1995**, *24*, 227–238. [CrossRef]
27. Si, C.Q.; Qi, F.; Ding, X.M.; He, F.; Gao, Z.J.; Feng, Q.; Zheng, L. CFD analysis of solar greenhouse thermal and humidity environment considering soil–crop–back wall interactions. *Energies* **2023**, *16*, 2305. [CrossRef]
28. Spalding, B.E.; Launderd, B. The numerical computation of turbulent flows. *Comput. Methods Appl. Mech. Eng.* **1974**, *3*, 269–289. [CrossRef]
29. Qin, Y.N.; Liang, Z. Design and simulation of air distribution in container mushroom house. *J. Anhui Agric. Sci.* **2025**, *53*, 190–194, 196. [CrossRef]
30. *NY/T 1451-2018*; Code for Ventilation Design of Greenhouse. Ministry of Agriculture of the People's Republic of China: Beijing, China, 2018.
31. Wells, C.M.; Amos, N.D. Design of air distribution systems for closed greenhouses. *Acta Hortic.* **1994**, *361*, 93–104. [CrossRef]
32. Miles, P.G.; Chang, S.-T. *Mushrooms: Cultivation, Nutritional Value, Medicinal Effect, and Environmental Impact*; CRC Press: Boca Raton, FL, USA, 2004.
33. Yang, K.; Shi, T.H.; Ming, T.Z.; Wu, Y.J.; Chen, Y.H.; Yu, Z.Y.; Ahmadi, M.H. Study of internal flow heat transfer characteristics of ejection-permeable FADS. *Energies* **2023**, *16*, 4377. [CrossRef]
34. Fang, H.; Wu, G.; Cheng, R.F.; Tong, Y.X. Numerical simulation of ventilation efficiency with perforated air tubes for controlling canopy environment in a plant factory based on CFD. *Trans. Chin. Soc. Agric. Eng.* **2021**, *37*, 188–193. [CrossRef]
35. Chen, C.H. A novel multi-criteria decision-making model for building material supplier selection based on Entropy-AHP weighted TOPSIS. *Entropy* **2020**, *22*, 259. [CrossRef]
36. Wang, Y.L.; Zhou, X.Y.; Liu, H.; Chen, X.C.; Yan, Z.X.; Li, D.X.; Liu, C.; Wang, J.R. Evaluation of the maturity of urban energy internet development based on AHP-entropy weight method and improved TOPSIS. *Energies* **2023**, *16*, 5151. [CrossRef]

Disclaimer/Publisher's Note: The statements, opinions and data contained in all publications are solely those of the individual author(s) and contributor(s) and not of MDPI and/or the editor(s). MDPI and/or the editor(s) disclaim responsibility for any injury to people or property resulting from any ideas, methods, instructions or products referred to in the content.